Joule, Volume *9*

Supplemental information

Solubilizing and stabilizing C_{60} with n-type polymer enables efficient inverted perovskite solar cells

Zhou Xing, Suxiang Ma, Bin-Wen Chen, Mingwei An, Ajuan Fan, Xinqiong Hu, Yang Wang, Lin-Long Deng, Qiufeng Huang, Hiroyuki Kanda, Fahad Gallab Al-Amri, Gainluca Pozzi, Yi Zhang, Jianxing Xia, Jiazhen Wu, Xugang Guo, and Mohammad Khaja Nazeeruddin

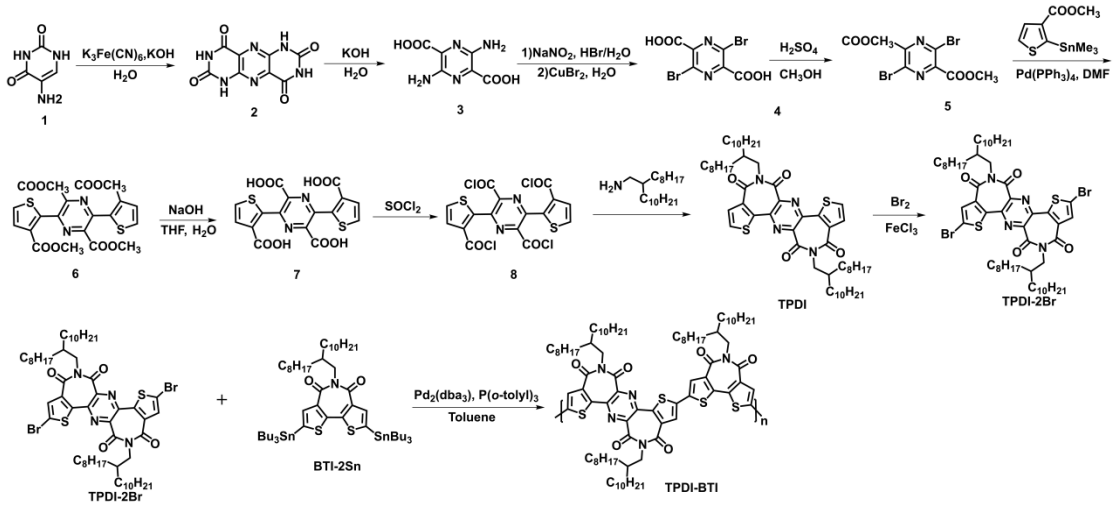

Scheme S1. Synthetic route of the TPDI-BTI.

Synthetic route of the TPDI-BTI (M_n = 6.3 kDa, PDI = 1.60). Detailed information can be found in the supplemental methods.

Supplemental methods

Synthetic details of the TPDI-BTI according to our previous work (*ACS Appl. Mater. Interfaces* 2023, 15, 1639)

Synthesis of 1,6-dihydropyrimido[4,5-g]pteridin-2,4,7,9-tetron (2).

5-aminourracil (10.0 g, 78.7 mmol) and KOH (17.8 g, 317 mmol) were dissolved in 200 mL of water and cooled to 8 °C. A 250 mL aqueous solution of potassium hexacyanoferrate (III) (81.6 g, 248 mmol) was added dropwise over the course of 1 h and stirred at room temperature for 1 h. The precipitate was collected by filtration and washed by using 1 M HCl. After drying, the product (1.5 g, yield: 16%) can be used in the next step without further purification.

Synthesis of 3,6-diaminopyrazine-2,5-dicarboxylic acid (3).

Compound **2** (0.44 g, 1.77 mmol) and 10 mL aqueous KOH (0.6 g, 10.64 mmol) solution were placed in an autoclave reaction vessel. Then the vessel was sealed in a vacuum oven and reacted at 170 °C under 7 atm. for 2 h. A bright yellow solution was then filtered and the pH was adjusted to ~3 by using 6 M HCl, resulting in the formation of a substantial amount of red precipitates, which was subsequently collected by filtration and dried in vacuum (0.25 g, yield: 45%).

Synthesis of 3,6-dibromopyrazine-2,5-dicarboxylic acid (4).

Compound **3** (0.10 g, 0.5 mmol) was dissolved in 3 mL hydrobromic acid (48%) and cooled to 0 °C. Then a solution of sodium nitrite (0.14 g, 2 mmol) in 5 mL of water was added. The mixture was stirred for 1 h at 0 °C and poured into a solution of cupric bromide (0.67 g, 3 mmol) in 20 mL of water following by stirring for another 3 h at room temperature. The aqueous solution was extracted for three times with ethyl acetate (EA), and the combined organic layer was dried over anhydrous sodium sulfate and filtered. After that, a pale-yellow solid product (45 mg, yield: 38%) was obtained, which can be used for the next step.

Synthesis of dimethyl 3,6-dibromopyrazine-2,5- dicarboxylate (5).

Compound **4** (0.5 g, 1.53 mmol) was dissolved in 30 mL methanol. Then 0.2 mL concentrated HCl (37%) was added into the reacting vessel, following by heating and stirring under reflux for 18 h. After that, the solvent was removed, and the residue was dissolved in saturated $NaHCO_3$ aqueous solution. The mixture was then extracted for three times with DCM, and the combined organic layer was dried over Na_2SO_4. The residue was purified by column chromatography on silica, yielding a white solid (0.21 g, 39%).

Synthesis of dimethyl 3,6-bis(3-(methoxycarbonyl)thiophen-2-yl)pyrazine-2,5-dicarboxylate (6).

Compound **5** (0.5 g, 1.41 mmol), methyl 2-(trimethylstannyl)thiophene-3-carboxylate (1.29 g, 4.24 mmol), $Pd(PPh_3)_4$ (50 mg) and DMF (7 mL) were added to an air-free reaction tube under a nitrogen atmosphere and was heated to 140 °C for 4 h under microwave irradiation. Once cooling to room temperature, the DMF was evaporated under a reduced pressure. The residue was purified by column chromatography over silica to obtain a white solid product (0.4 g, yield: 40%).

Synthesis of 3,6-bis(3-carboxythiophen-2-yl)pyrazine-2,5-dicarboxylic acid (7).

Compound **6** (0.9 g, 1.89 mmol), KOH (1.06 g, 18.9 mmol), THF (25 mL), H_2O (5 mL) and EtOH (25 mL) were added to a round bottom flask, and was refluxed overnight. After cooling to room temperature, the solvent was removed under a reduced pressure. The residue was then cooled to 0 °C, and 10 mL of dilute

HCl was added into the vessel. The resulting precipitate was filtered and washed with 30 mL H_2O, yielding compound **7** (0.85 g, yield: 98%).

Synthesis of 3,6-bis(3-(chlorocarbonyl)thiophen-2-yl)pyrazine-2,5-dicarbonyl dichloride (8).
Compound **7** (1 g, 2.38 mmol) and 6 mL of thionyl chloride ($SOCl_2$, 82.6 mmol) were added to a round bottom flask, and was heated to 80 °C overnight. The excess solvent was then evaporated under a reduced pressure. The crude compound **8** can be used directly in the next step.

Synthesis of TPDI.
A mixture of 2-octyldodecan-1-amine (1.44 g, 4.87 mmol) and compound **8** (2.38 mmol) was heated to 120 °C for 3 h. After cooling to room temperature, the reaction mixture was purified by silica gel column chromatography. A yellow solid was obtained (0.22 g, yield: 10%).

Synthesis of TPDI-2Br.
The mixture of compound **TPDI** (0.2 g, 0.21 mmol), iron (III) chloride (5 mg) and Br_2 were dissolved in $CHCl_3$, and then heated to 60 °C and stirred overnight. After cooling to room temperature, an aqueous solution of Na_2SO_3 was added while stirring. The reaction mixture was extracted for three times with DCM, and the combined organic layer was dried over anhydrous Na_2SO_4 and filtrated. The solvent was removed under reduced pressure to obtain a yellow solid, which was then purified by silica gel column chromatography (46 mg, yield: 20%).

Synthesis of polymer TPDI-BTI.
To a flame-dried glass tube were added with TPDI-2Br (53.3 mg, 0.0484 mmol), distannylated BTI (52.9 mg, 0.0484 mmol), $Pd_2(dba)_3$ (0.66 mg, 0.000726 mmol), and P(*o*-tolyl)$_3$ (1.76 mg, 0.0058 mmol). The tube was stirred at 140 °C for 3h under microwave irradiation. Subsequently, 0.1 mL of 2-(tributylstanny)thiophene and 0.2 mL of 2-bromothiophene were added together and stirred at 110 °C for 0.5 h. After cooling to room temperature, the solution was dropped into 100 mL methanol. The formed precipitates were collected and subjected to Soxhlet extraction by using methanol, acetone, hexane, dichloromethane and chloroform. The final chloroform fraction was concentrated and precipitated into methanol. Ultimately, the solid was collected and dried under vacuum to obtain the polymeric product, TPDI-BTI (56 mg, yield: 83%).

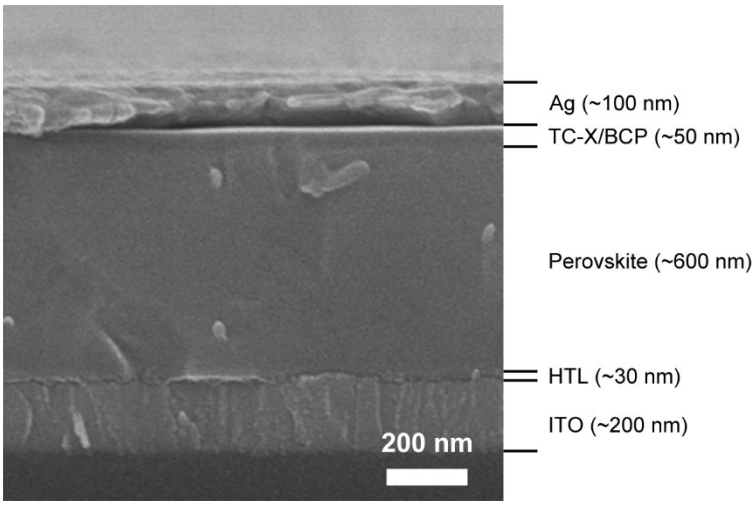

Figure S1. SEM image of the device.

Enlarged view of cross-sectional SEM image of the device.

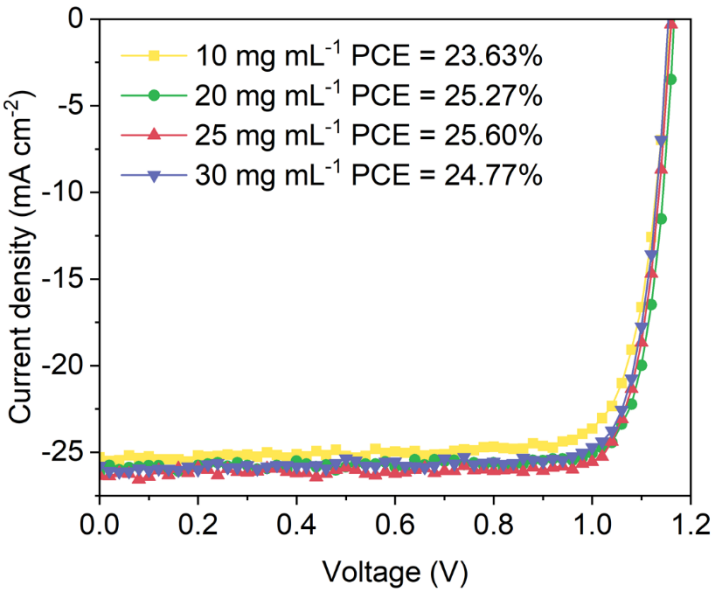

Figure S2. Photovoltaic performance of different TC-5 devices.

J-V curves of the TC-5 ETLs fabricated by different concentrations of TPDI-BTI-C_{60} precursor solutions.

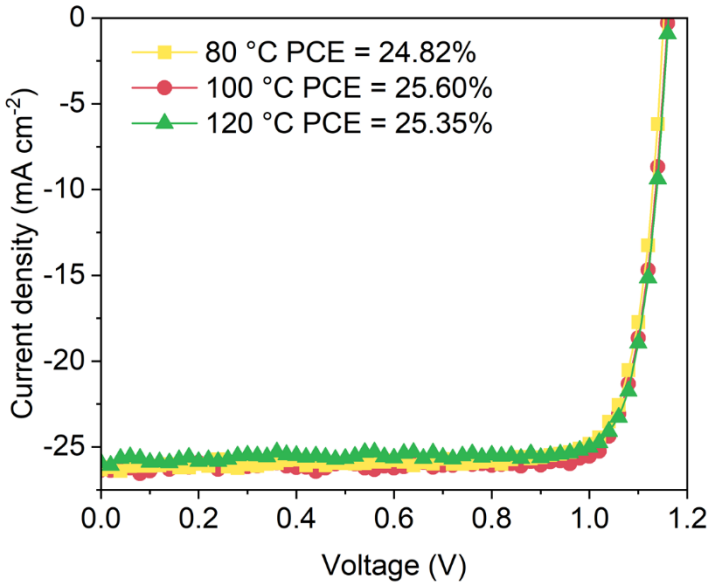

Figure S3. Photovoltaic performance of different TC-5 devices.
J-V curves of the TC-5 ETLs annealed at different temperatures.

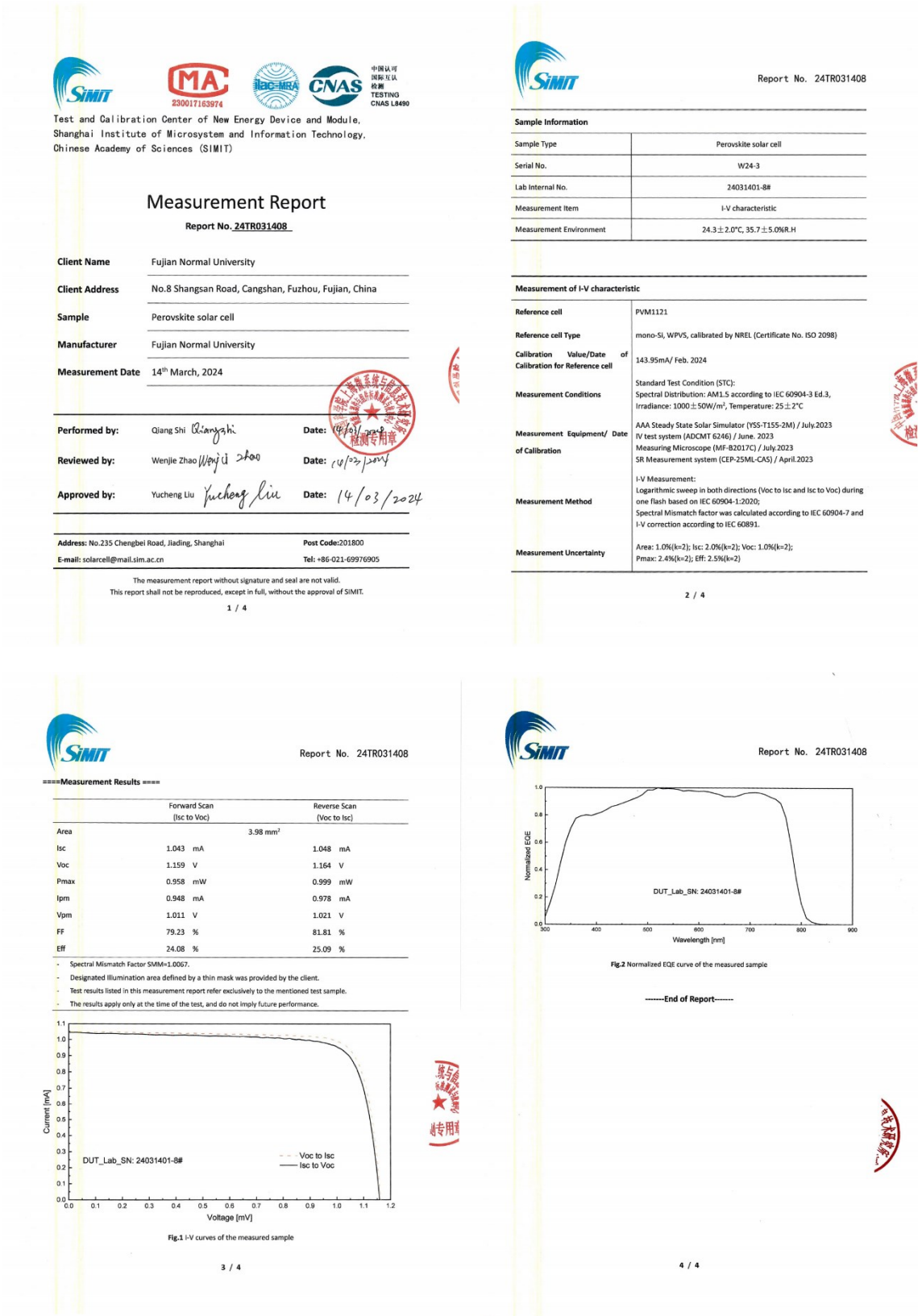

Test and Calibration Center of New Energy Device and Module,
Shanghai Institute of Microsystem and Information Technology,
Chinese Academy of Sciences (SIMIT)

Measurement Report

Report No. 24TR031408

Client Name	Fujian Normal University
Client Address	No.8 Shangsan Road, Cangshan, Fuzhou, Fujian, China
Sample	Perovskite solar cell
Manufacturer	Fujian Normal University
Measurement Date	14th March, 2024

Performed by:	Qiang Shi	**Date:** 14/03/2024
Reviewed by:	Wenjie Zhao	**Date:** 14/03/2024
Approved by:	Yucheng Liu	**Date:** 14/03/2024

Address: No.235 Chengbei Road, Jiading, Shanghai **Post Code:**201800
E-mail: solarcell@mail.sim.ac.cn **Tel:** +86-021-69976905

The measurement report without signature and seal are not valid.
This report shall not be reproduced, except in full, without the approval of SIMIT.

1 / 4

Report No. 24TR031408

Sample Information

Sample Type	Perovskite solar cell
Serial No.	W24-3
Lab Internal No.	24031401-8#
Measurement Item	I-V characteristic
Measurement Environment	24.3±2.0°C, 35.7±5.0%R.H

Measurement of I-V characteristic

Reference cell	PVM1121
Reference cell Type	mono-Si, WPVS, calibrated by NREL (Certificate No. ISO 2098)
Calibration Value/Date of Calibration for Reference cell	143.95mA/ Feb. 2024
Measurement Conditions	Standard Test Condition (STC): Spectral Distribution: AM1.5 according to IEC 60904-3 Ed.3, Irradiance: 1000±50W/m², Temperature: 25±2°C
Measurement Equipment/ Date of Calibration	AAA Steady State Solar Simulator (YSS-T155-2M) / July.2023 IV test system (ADCMT 6246) / June. 2023 Measuring Microscope (MF-B2017C) / July.2023 SR Measurement system (CEP-25ML-CAS) / April.2023
Measurement Method	I-V Measurement: Logarithmic sweep in both directions (Voc to Isc and Isc to Voc) during one flash based on IEC 60904-1:2020; Spectral Mismatch factor was calculated according to IEC 60904-7 and I-V correction according to IEC 60891.
Measurement Uncertainty	Area: 1.0%(k=2); Isc: 2.0%(k=2); Voc: 1.0%(k=2); Pmax: 2.4%(k=2); Eff: 2.5%(k=2)

2 / 4

Report No. 24TR031408

====Measurement Results ====

	Forward Scan (Isc to Voc)	Reverse Scan (Voc to Isc)
Area	3.98 mm²	
Isc	1.043 mA	1.048 mA
Voc	1.159 V	1.164 V
Pmax	0.958 mW	0.999 mW
Ipm	0.948 mA	0.978 mA
Vpm	1.011 V	1.021 V
FF	79.23 %	81.81 %
Eff	24.08 %	25.09 %

- Spectral Mismatch Factor SMM=1.0067.
- Designated Illumination area defined by a thin mask was provided by the client.
- Test results listed in this measurement report refer exclusively to the mentioned test sample.
- The results apply only at the time of the test, and do not imply future performance.

Fig.1 I-V curves of the measured sample

3 / 4

Report No. 24TR031408

Fig.2 Normalized EQE curve of the measured sample

-------End of Report-------

4 / 4

Figure S4. Certification report of the top-performing TC-5 device.

Certified performance of the top-performing TC-5 device from the accredited independent photovoltaic calibration laboratory, Shanghai Institute of Microsystem and Information Technology, Chinese Academy of Sciences (SIMIT). This report was produced with the permission of SIMIT.

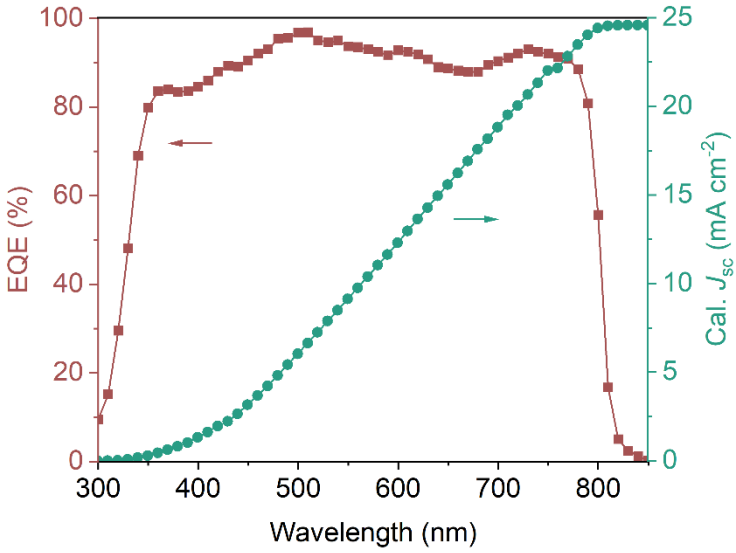

Figure S5. External quantum efficiency measurement of the TC-5 device.
External quantum efficiency spectra and the calculated J_{sc} value of the TC-5 device.

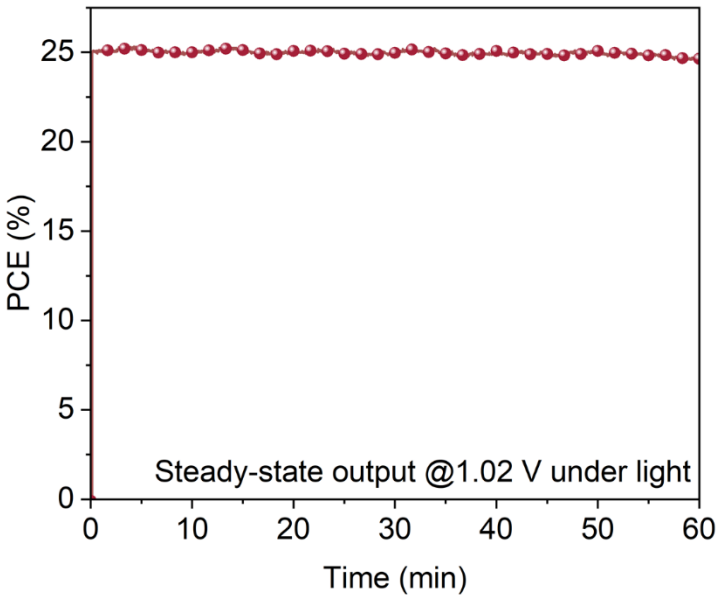

Figure S6. Steady-state output performance of the TC-5 device.

Steady-state output performance at maximum power point of the TC-5 device.

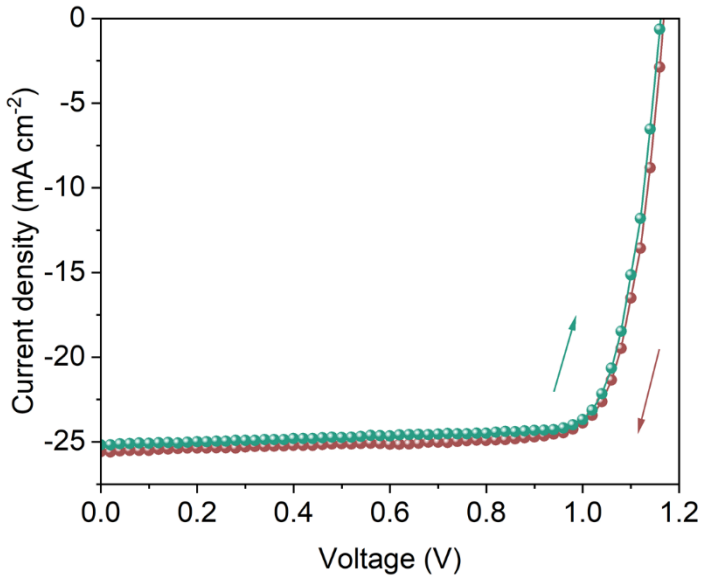

Figure S7. Hysteresis test of the TC-5 device.

J-V curves of the TC-5 device under different scanning directions.

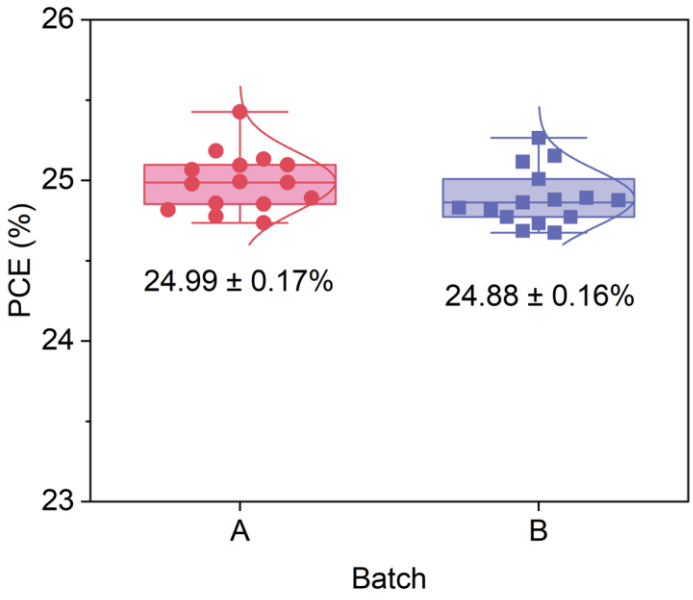

Figure S8. Comparison of the PCE of different TC-5 devices.

Comparison of the PCE for the TC-5 devices based on different batches of the TPDI-BTI (Batch A was synthesized in 2023 and Batch B was synthesized in 2024).

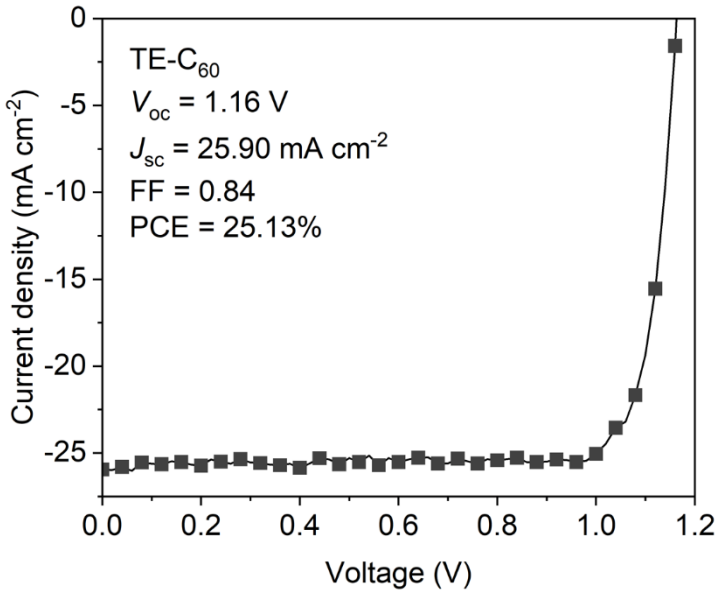

Figure S9. Photovoltaic performance of the TE-C_{60} device.

J-V curve and photovoltaic parameters of the TE-C_{60} device (TE-C_{60} represents for the thermally-evaporated C_{60} film).

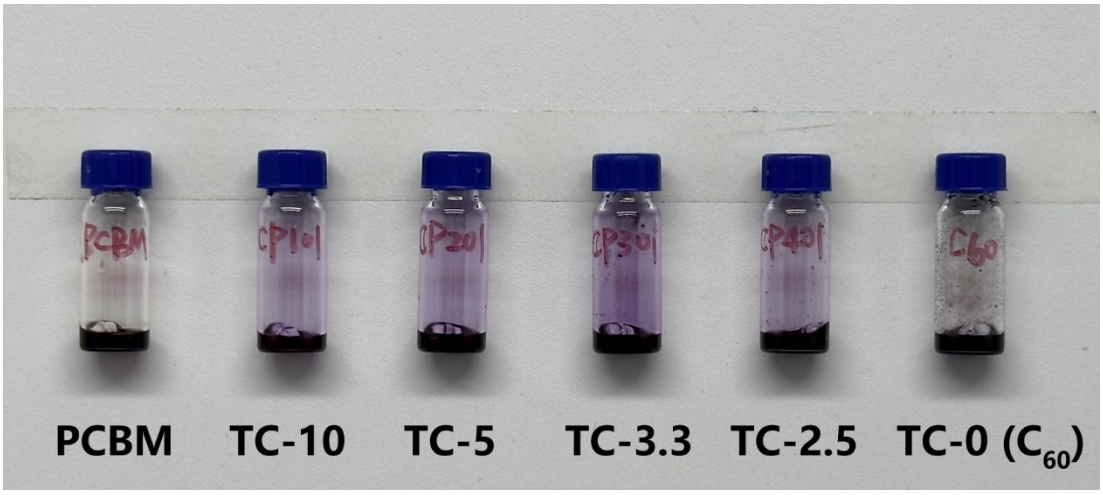

Figure S10. Soluble situation of different samples.

The soluble situation of TC-0 (C_{60}-only), TC-2.5, TC-3.3, TC-5, TC-10 and PCBM under the same concentration of 25 mg mL^{-1} with the DCB solvent. PCBM (99.5%) and C_{60} (99.9%) powders are obtained from commercial channels.

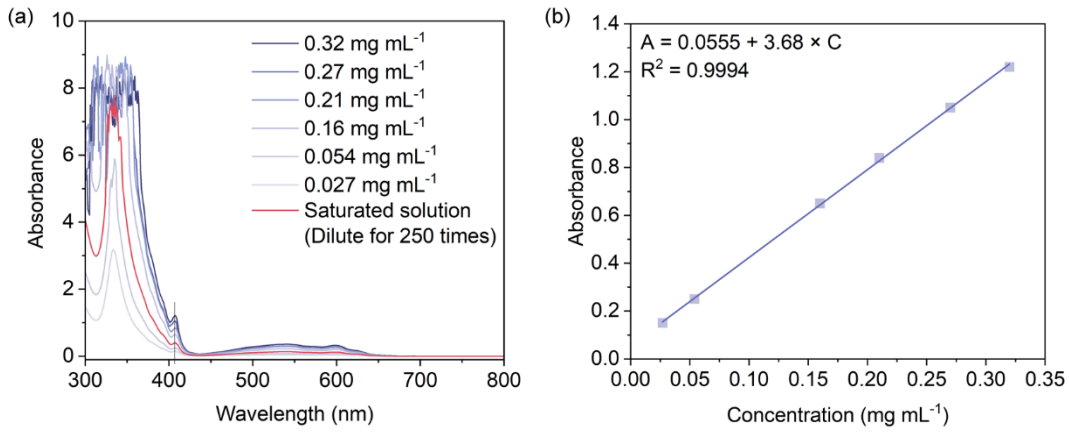

Figure S11. Solubility test of C_{60}.

(a) UV-Vis absorption spectra of C_{60} solutions with different concentrations. (b) The fitted line and equation of the Absorbance points. The absorption value of saturated solution at 407 nm is 0.40.

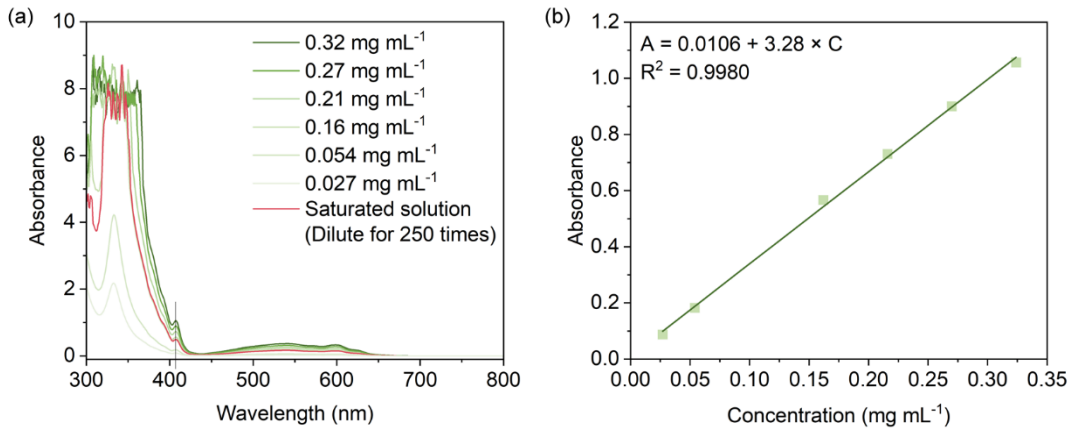

Figure S12. Solubility test of C_{60} in TC-5 sample.

(a) UV-Vis absorption spectra of TC-5 solutions with different concentrations. (b) The fitted line and equation of the Absorbance points. The absorption value of saturated solution at 407 nm is 0.47.

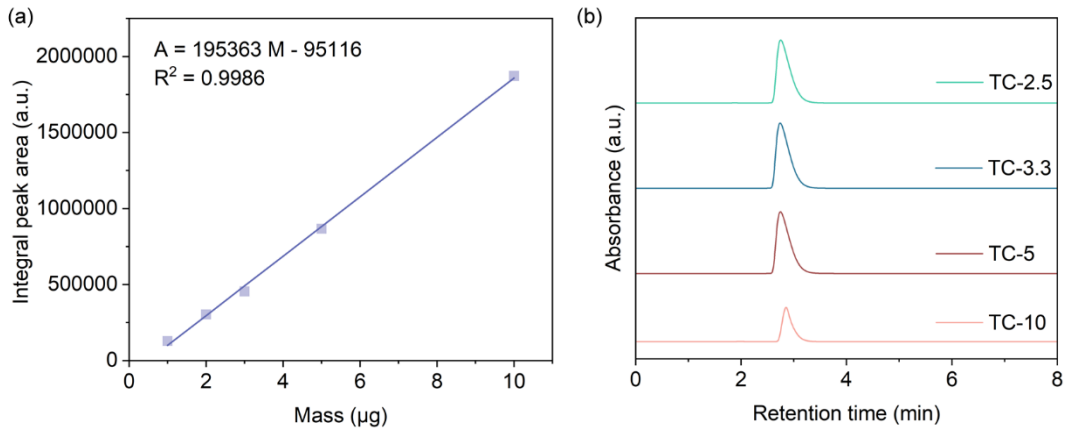

Figure S13. HPLC analysis of different samples.

(a) Relation between the integral peak areas and the mass of C_{60} obtained from HPLC. (b) HPLC chromatogram for the separation of mixed solutions washed off from the TC-X films.

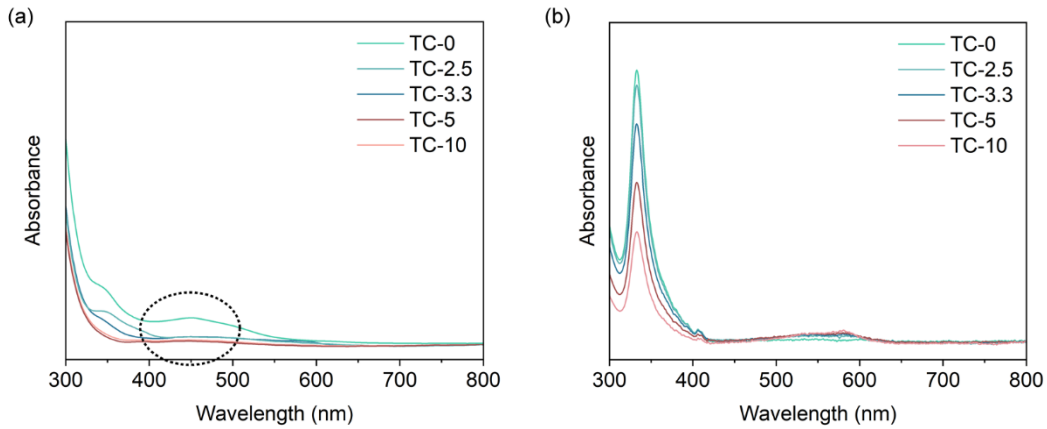

Figure S14. UV-Vis spectra of different samples.

UV-Vis spectra of the TC-0, TC-2.5, TC-3.3, TC-5 and TC-10 in (a) thin-film state and (b) solution state, respectively.

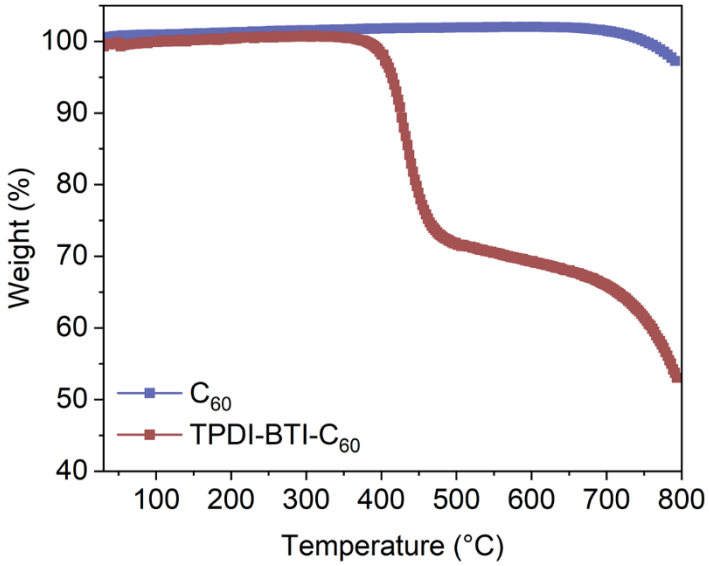

Figure S15. Thermogravimetric analysis of different samples.
Thermogravimetric analysis of (a) C_{60} and (b) TPDI-BTI-C_{60}, respectively.

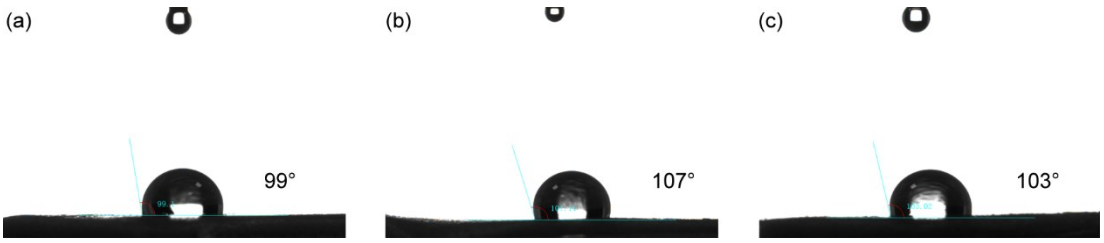

Figure S16. Water contact angle measurements of different films.

Water contact angle measurements of (a) C_{60}, (b) TPDI-BTI, and (c) TC-5 films, respectively.

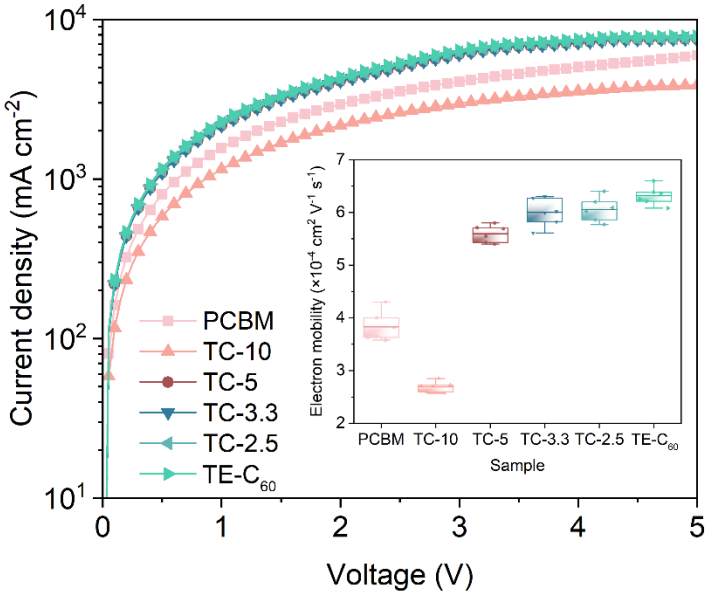

Figure S17. *J-V* curves of different electron-only devices.

J-V curves of different electron-only devices based on the PCBM, TE-C_{60}, TC-2.5, TC-3.3, TC-5 and TC-10 films. Inset is the statistical electron mobility values of different films. (TE-C_{60} represents for the thermally-evaporated-C_{60} film)

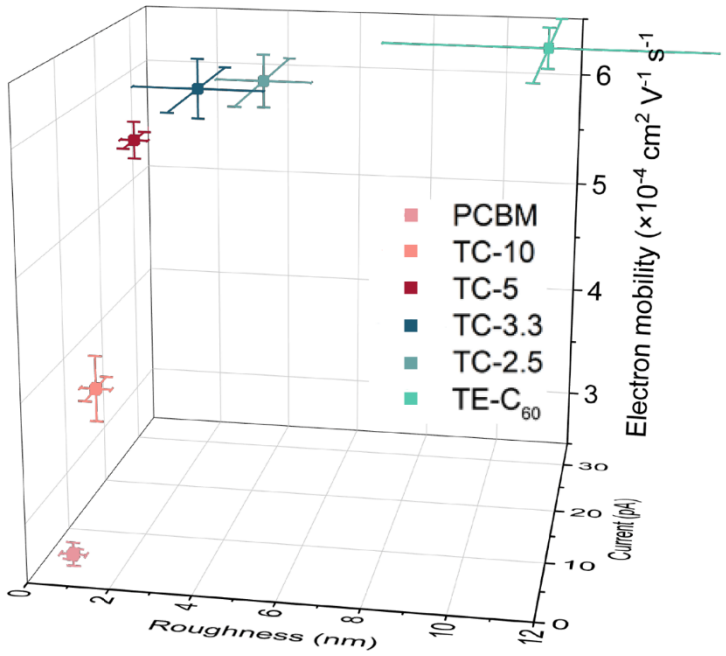

Figure S18. Relations between roughness, surface current and electron mobility of different films. Diagram combining roughness, surface current and electron mobility values of PCBM, TE-C_{60}, TC-2.5, TC-3.3, TC-5 and TC-10 films. (TE-C_{60} represents for the thermally-evaporated C_{60} film)

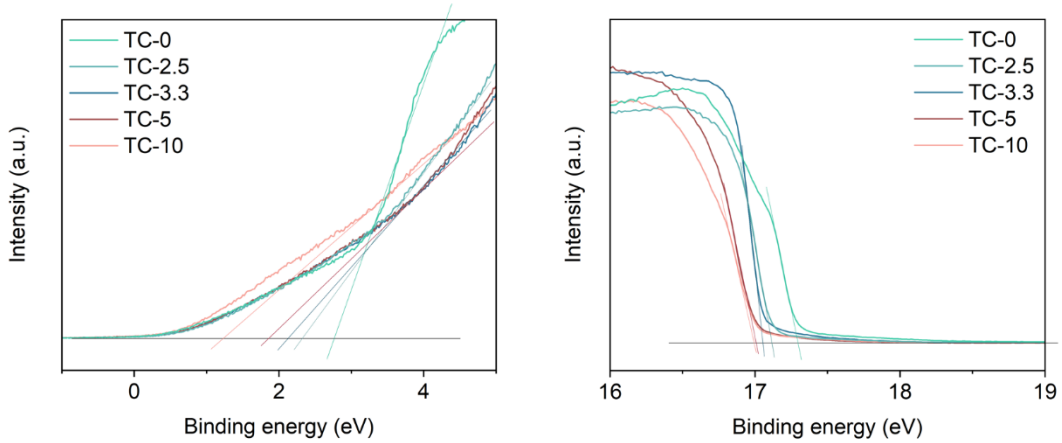

Figure S19. UPS spectra of different films.

UPS spectra of the TC-0, TC-2.5, TC-3.3, TC-5 and TC-10 films.

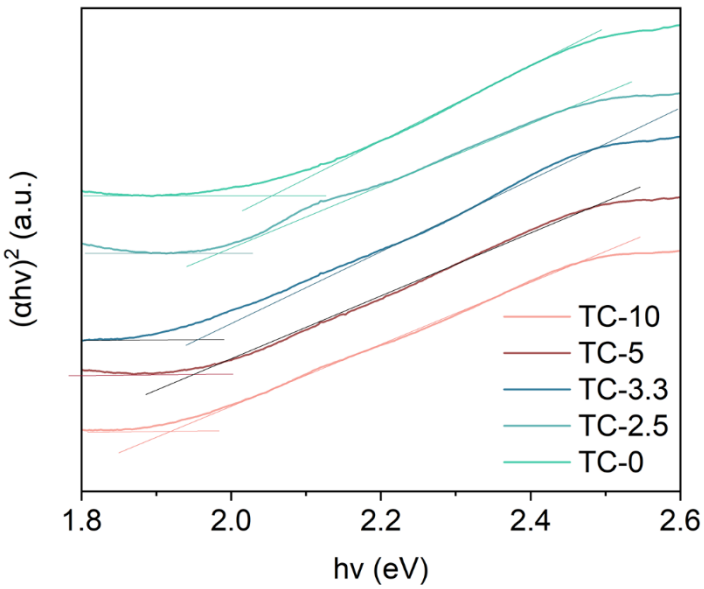

Figure S20. Tauc plots of different films.

Tauc plots of the TC-0, TC-2.5, TC-3.3, TC-5 and TC-10 films.

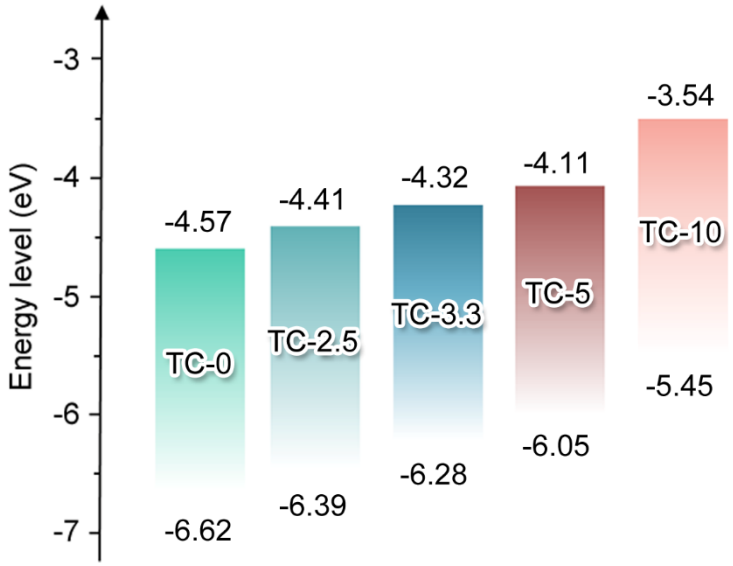

Figure S21. Calculated energy levels of different ETLs.

Energy levels of the TC-0, TC-2.5, TC-3.3, TC-5 and TC-10 films calculated by UPS spectra and Tauc plots.

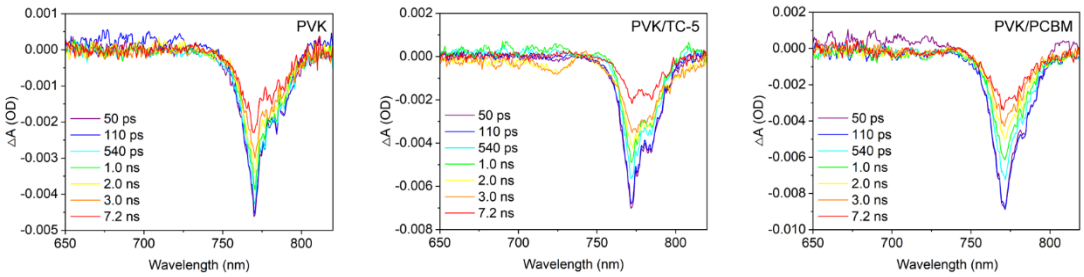

Figure S22. TAS curves of different films.

TAS curves of perovskite, perovskite/TC-5 and perovskite/PCBM films recorded at different delay times.

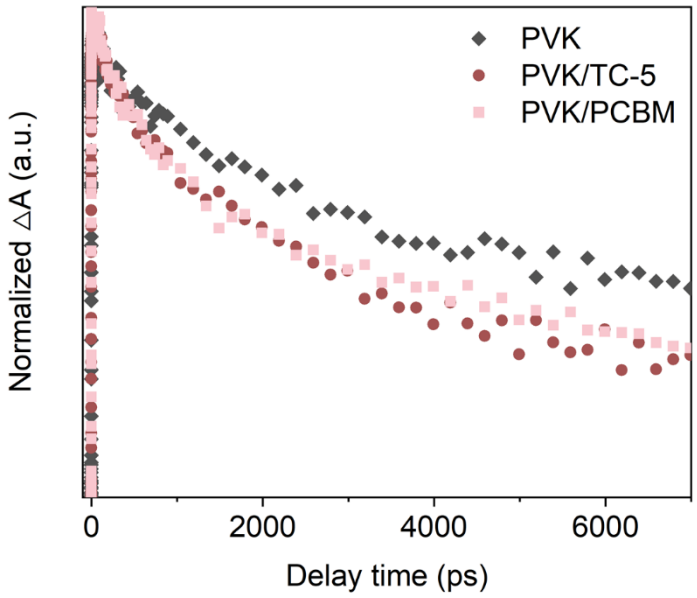

Figure S23. TAS signal decay traces of different samples.

TAS signal decay traces of the GSB peaks of perovskite, perovskite/TC-5 and perovskite/PCBM films.

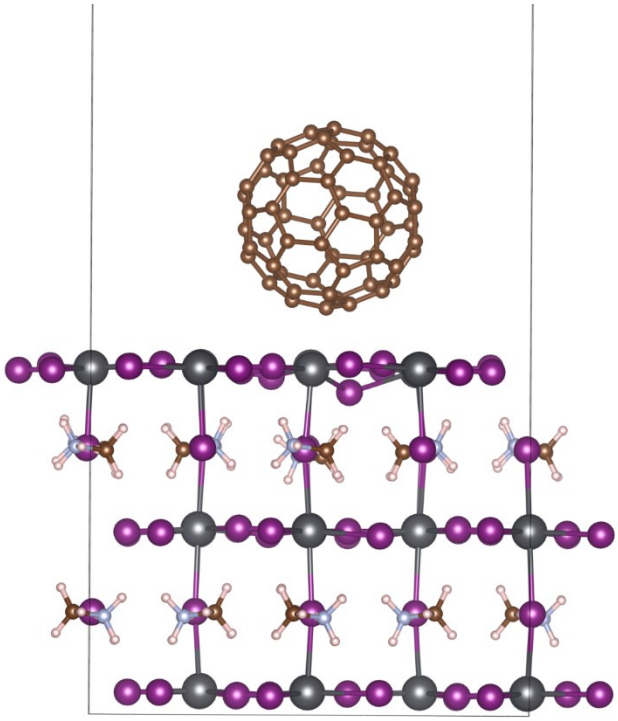

Figure S24. Simulated interacting situation of C_{60}-perovskite.
The simulated interacting situation between C_{60} molecule and perovskite surface visualized from the back view. (Brown: carbon, purple: iodine, grey: lead, blue: nitrogen, white: hydrogen)

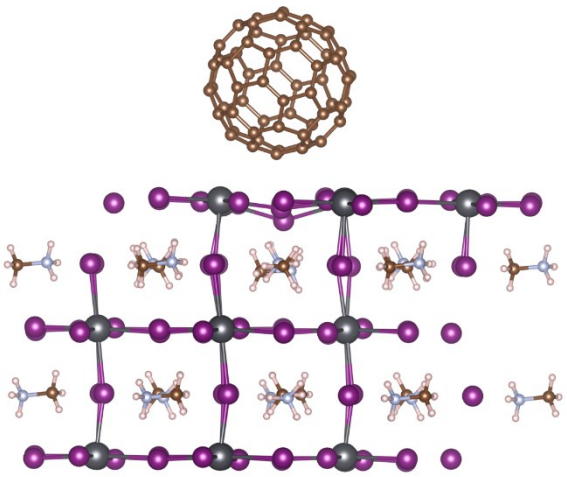

Figure S25. Simulated interacting situation of C_{60}-perovskite.
The simulated interacting situation between C_{60} molecule and perovskite surface visualized from the front view. (Brown: carbon, purple: iodine, grey: lead, blue: nitrogen, white: hydrogen)

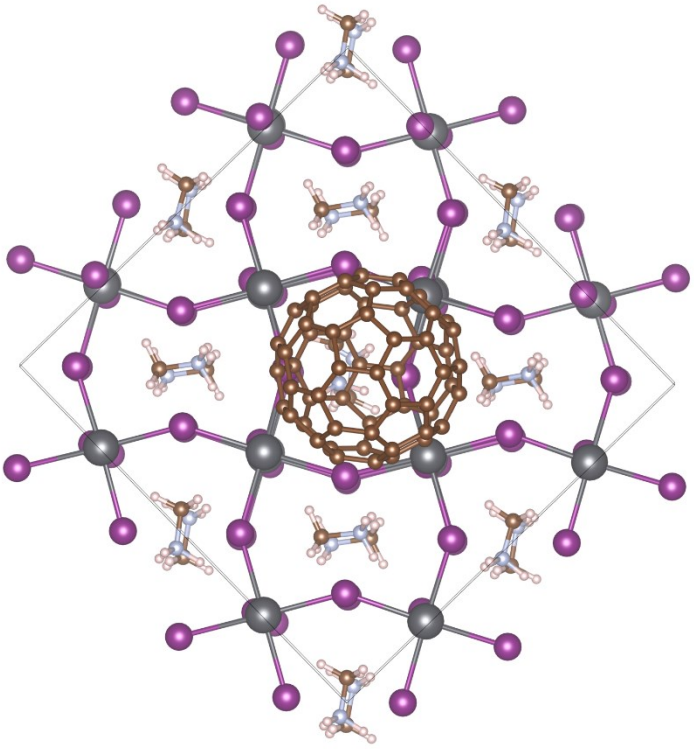

Figure S26. Simulated interacting situation of C_{60}-perovskite.
The simulated interacting situation between C_{60} molecule and perovskite surface visualized from the top view. (Brown: carbon, purple: iodine, grey: lead, blue: nitrogen, white: hydrogen)

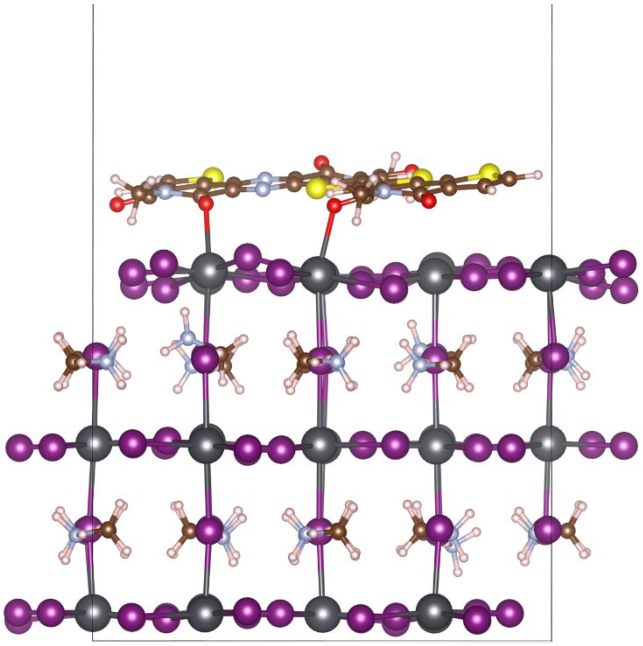

Figure S27. Simulated interacting situation of TPDI-BTI-perovskite.
The simulated interacting situation between TPDI-BTI monomer and perovskite surface visualized from the back view. (Brown: carbon, purple: iodine, grey: lead, blue: nitrogen, white: hydrogen, red: oxygen, yellow: sulfur)

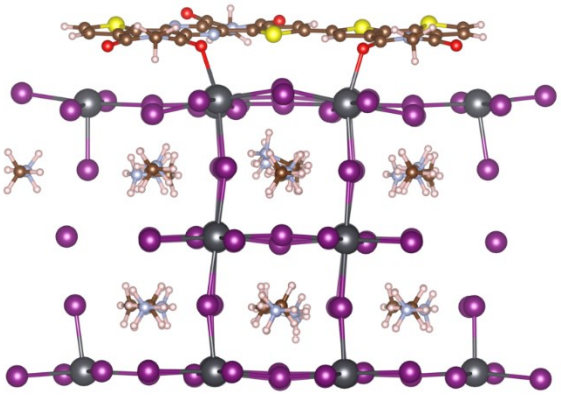

Figure S28. Simulated interacting situation of TPDI-BTI-perovskite.
The simulated interacting situation between TPDI-BTI monomer and perovskite surface visualized from the front view. (Brown: carbon, purple: iodine, grey: lead, blue: nitrogen, white: hydrogen, red: oxygen, yellow: sulfur)

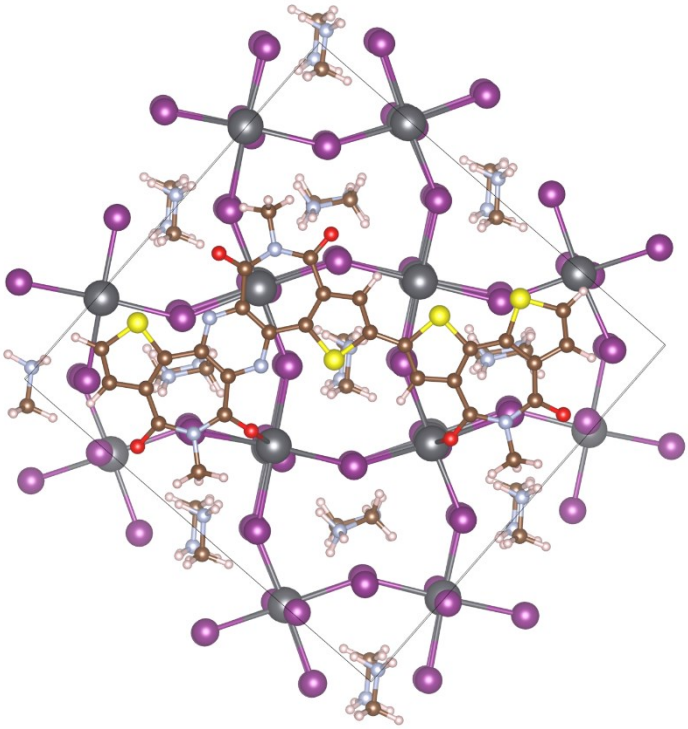

Figure S29. Simulated interacting situation of TPDI-BTI-perovskite.
The simulated interacting behavior between TPDI-BTI monomer and perovskite surface visualized from the top view. (Brown: carbon, purple: iodine, grey: lead, blue: nitrogen, white: hydrogen, red: oxygen, yellow: sulfur)

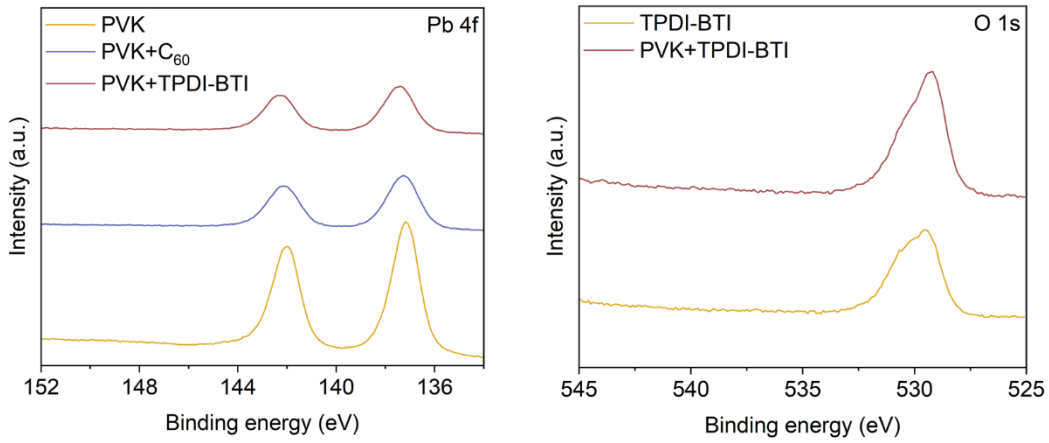

Figure S30. XPS spectra of different samples.

The XPS spectra of perovskite, perovskite+C_{60}, perovskite+TPDI-BTI and TPDI-BTI samples.

Table S1. Photovoltaic parameters of different TC-X devices. Listed in the brackets were the parameters of each champion devices.

ETL	V_{oc} (V)	J_{sc} (mA cm^{-2})	FF	PCE (%)
TC-10	1.09±0.01 (1.09)	23.67±0.66 (24.68)	0.79±0.01 (0.80)	20.57±0.55 (21.53)
TC-3.3	1.15±0.01 (1.15)	25.20±0.26 (25.53)	0.79±0.01 (0.80)	22.99±0.29 (23.49)
TC-2.5	1.10±0.01 (1.10)	24.64±0.63 (25.31)	0.80±0.01 (0.80)	21.55±0.59 (22.27)

Table S2. Photovoltaic parameters of different TC-X devices. Listed in the brackets were the parameters of each champion devices. (Type 1: $MAPbI_3$, Type 2: $Cs_{0.05}(FA_{0.92}MA_{0.08})_{0.95}Pb(I_{0.92}Br_{0.08})_3$, Type 3: $Cs_{0.05}(FA_{0.95}MA_{0.05})_{0.95}Pb(I_{0.95}Br_{0.05})_3$)

ETL	Perovskite	V_{oc} (V)	J_{sc} (mA cm^{-2})	FF	PCE (%)
PCBM	Type 1	1.12±0.01	23.76±0.28	0.81±0.02	21.51±0.24
		(1.13)	(23.63)	(0.82)	(21.87)
PCBM	Type 2	1.16±0.01	24.50±0.21	0.81±0.01	23.14±0.36
		(1.15)	(24.68)	(0.84)	(23.77)
PCBM	Type 3	1.14±0.01	24.67±0.22	0.81±0.01	22.89±0.34
		(1.14)	(24.65)	(0.82)	(23.14)
TC-5	Type 1	1.13±0.02	24.57±0.59	0.80±0.02	22.30±0.71
		(1.13)	(24.19)	(0.82)	(22.39)
TC-5	Type 2	1.16±0.01	26.22±0.18	0.82±0.01	25.06±0.19
		(1.16)	(26.38)	(0.84)	(25.60)
TC-5	Type 3	1.15±0.01	24.90±0.92	0.82±0.03	23.36±0.33
		(1.15)	(26.14)	(0.79)	(23.66)
TC-0	Type 1	0.89±0.12	21.37±1.53	0.54±0.07	10.05±0.85
		(1.04)	(23.43)	(0.53)	(11.54)
TC-0	Type 2	0.98±0.09	24.13±0.99	0.59±0.05	13.77±0.41
		(1.06)	(22.15)	(0.63)	(14.65)
TC-0	Type 3	0.95±0.07	23.37±2.05	0.53±0.17	12.69±0.49
		(1.05)	(20.68)	(0.63)	(13.68)

Table S3. The comparison of device PCE between this work and literatures. (SP and TE represents for solution-processed and thermally-evaporated, respectively)

Method	Device structure	PCE (%)	Ref.
SP	ITO/PEDOT:PSS/PVK/**C_{60}**/BCP/Al	3.0	Adv. Mater. [S1]
SP	ITO/PEDOT:PSS/PVK/**C_{60}**/bis-C_{60}/Ag	15.44	Adv. Energy Mater. [S2]
SP	ITO/PEDOT:PSS/PVK/**C_{60}:C_{70}**/Ag	14.04	J. Power Sources [S3]
SP	ITO/**C_{60}:C_{70}**/PVK/spiro-OMeTAD/Au	16.7	ACS Appl. Mater. Interfaces [S4]
SP	ITO/PEDOT:PSS/PVK/**C_{60}:C_{70}**/BCP/Ag	15.8	ACS Appl. Mater. Interfaces [S4]
SP	ITO/**C_{60}**/C_{60}-NPs/PVK/spiro-OMeTAD/Au	19.45	J. Mater. Chem. A [S5]
SP	ITO/NiO_x/PVK/**ZnO@C_{60}:TPFPB:$LiClO_4$**/Ag	15.19	Adv. Mater. [S6]
SP	ITO/**C_{60}:DBU**/PVK/spiro-OMeTAD/Au	19.98	J. Mater. Chem. C [S7]
SP	FTO/NiO_x/PVK/**C_{60}:Co-TiO_2**/BCP/Ag	22.13	Adv. Sci. [S8]
SP	ITO/**C_{60}:APTES**/PVK/C	18.64	Angew. Chem. Int. Ed. [S9]
SP	ITO/PTAA/PVK/**C_{60}:$PC_{61}BM$**/BCP/Ag	19.8	Chem. Eng. J. [S10]
SP	ITO/NiO_x/PTAA/PVK/**CC2**/BCP/Ag	21.7	Angew. Chem. Int. Ed. [S11]
TE	ITO/2PACz/PVK/**C_{60}**/BCP/Ag	24.3	Science [S12]
TE	ITO/P3CT-N/PVK/**C_{60}**/BCP/Ag	23.5*	Science [S13]
TE	ITO/PTAA/PVK/**C_{60}**/BCP/Ag	24.3*	Science [S14]
TE	ITO/NiO_x/PVK/**C_{60}**/BCP/Ag	24.7	Energy Environ. Sci. [S15]
TE	ITO/2PACz/PVK/**C_{60}**/SnO_x/Ag	24.2*	Joule [S16]
TE	ITO/Me-4PACz/PVK/**C_{60}**/BCP/Ag	24.5	Nat. Energy [S17]
TE	ITO/MeO-2PACz/PVK/**C_{60}**/BCP/Ag	24.2*	Science [S18]
TE	ITO/Me-4PACz/PVK/**C_{60}**/BCP/Ag	24.7*	Science [S19]
TE	ITO/PTAA/PVK/LiF/**C_{60}**/SnO_2/ITO/Cu	24.5	Nat. Energy [S20]
TE	ITO/2PACz/PVK/**C_{60}**/BCP/Ag	25.0*	Nature [S21]
TE	ITO/ATO_x/SAM/PVK/**C_{60}**/BCP/Ag	25.06*	Nat. Energy [S22]
SP	ITO/NiO_x/Me-4PACz/PVK/**TC-5**/BCP/Ag	25.60	This work
SP	ITO/NiO_x/Me-4PACz/PVK/**TC-5**/BCP/Ag	25.09*	This work

* Certified PCE

Table S4. The integral peak area of HPLC chromatogram for the TC-X and calculated compositions in thin-film state.

Film	Integral peak area of C_{60}	Mass of C_{60} μg /100 μL	Mass of TPDI-BTI μg /100 μL	Weight ratio TPDI-BTI/(TPDI-BTI+C_{60})
TC-10	11265118	58	8	13.8%
TC-5	13216468	68	4	5.9%
TC-3.3	13355633	69	2.64	3.8%
TC-2.5	13956318	71	2	2.8%

Table S5. Different statistical data of the TC-X films.

Sample	Roughness (nm)	Current (pA)	Electron mobility ($\times 10^{-4}$ cm^2 V^{-1} s^{-1})
PCBM	0.99±0.39	8.17±2.76	3.83±0.28
TC-10	0.98±0.32	1.71±0.90	2.69±0.10
TC-5	0.94±0.36	20.45±3.08	5.60±0.16
TC-3.3	2.39±1.73	23.38±9.47	6.00±0.26
TC-2.5	4.00±1.26	25.19±10.36	6.05±0.23
TC-0	11.22±4.37	30.18±15.03	6.32±0.18

Table S6. Specific molecular energy between different molecules.

Sample A-B	A (eV)	B (eV)	Theoretical A+B (eV)	Actual A+B (eV)	E_{int}* (eV)
C_{60}-C_{60}	-557.7003765	-557.7005714	-1115.400948	-1115.458975	-0.058
TPDI-BTI-TPDI-BTI	-468.0221698	-468.0689433	-936.0911131	-936.4554975	-0.364
C_{60}-TPDI-BTI	-557.7459665	-467.9118075	-1025.657774	-1026.253785	-0.596

* E_{int} = (Actual A+B) — (Theoretical A+B)

Supplemental references

[S1] J.-Y. Jeng *et al.* $CH_3NH_3PbI_3$ perovskite/fullerene planar-heterojunction hybrid solar cells. *Adv. Mater.* **25**, 3727-3732 (2013).

[S2] P.-W. Liang *et al.* Roles of fullerene-based interlayers in enhancing the performance of organometal perovskite thin-film solar cells. *Adv. Energy Mater.* **5**, 1402321 (2015).

[S3] S.-M Dai *et al.* Pristine fullerenes mixed by vacuum-free solution process: Efficient electron transport layer for planar perovskite solar cells. *J. Power Sources* **339**, 27-32 (2017).

[S4] H.-S. Lin *et al.* Achieving high efficiency in solution-processed perovskite solar cells using C_{60}/C_{70} mixed fullerenes. *ACS Appl. Mater. Interfaces* **10**, 39590-39598 (2018).

[S5] X. Zhao *et al.* Room-temperature-processing fullerene single-crystalline nanoparticles for high-performance flexible perovskite photovoltaics. *J. Mater. Chem. A* **7**, 1509-1518 (2019).

[S6] C. Liu *et al.* Tailoring C_{60} for efficient inorganic $CsPbI_2Br$ perovskite solar cells and modules. *Adv. Mater.* **32**, 1907361 (2020).

[S7] X. He *et al.* High-efficiency and UV-stable flexible perovskite solar cells enabled by an alkaloid-doped C_{60} electron transport layer. *J. Mater. Chem. C* **8**, 10401-10407 (2020).

[S8] X. Hu *et al.* 22% efficiency inverted perovskite photovoltaic cell using cation-doped brookite TiO_2 top buffer. *Adv. Sci.* **7**, 2001285 (2020).

[S9] T. Tian *et al.* Interfacial linkage and carbon encapsulation enable full solution-printed perovskite photovoltaics with prolonged lifespan. *Angew. Chem. Int. Ed.* **60**, 23735-23742 (2021).

[S10] Z. Jia *et al.* Precursor formula engineering enabling high quality solution processed C_{60} films for efficient and stable inverted perovskite solar cells. *Chem. Eng. J* **446**, 136897 (2022).

[S11] Z. Xing *et al.* Bowl-assisted ball assembly for solvent-processing the C_{60} electron transport layer of high-performance inverted perovskite solar cell. *Angew. Chem. Int. Ed.* **62**, e202305357 (2023).

[S12] R. Azmi *et al.* Damp heat-stable perovskite solar cells with tailored-dimensionality 2D/3D heterojunctions. *Science* **376**, 73-77 (2022).

[S13] X. Li *et al.* Constructing heterojunctions by surface sulfidation for efficient inverted perovskite solar cells. *Science* **375**, 434-437 (2022).

[S14] Z. Li *et al.* Organometallic-functionalized interfaces for highly efficient inverted perovskite solar cells. *Science* **376**, 416-420 (2022).

[S15] Y. Huang *et al.* Finite perovskite hierarchical structures via ligand confinement leading to efficient inverted perovskite solar cells. *Energy Environ. Sci.* **16**, 557-564 (2023).

[S16] Z. Zhu *et al.* Correlating the perovskite/polymer multi-mode reactions with deep-level traps in perovskite solar cells. *Joule* **6**, 2849-2868 (2022).

[S17] X. Zheng *et al.* Co-deposition of hole-selective contact and absorber for improving the processability of perovskite solar cells. *Nat. Energy* **8**, 462-472 (2023).

[S18] G. Li *et al.* Highly efficient p-i-n perovskite solar cells that endure temperature variations. *Science* **379**, 399-403 (2023).

[S19] W. Peng *et al.* Reducing nonradiative recombination in perovskite solar cells with a porous insulator contact. *Science* **379**, 683-690 (2023).

[S20] N. Li *et al.* Barrier reinforcement for enhanced perovskite solar cell stability under reverse bias. *Nat. Energy* **9**, 1264-1274(2024).

[S21] R. Azmi *et al.* Double-side 2D/3D heterojunctions for inverted perovskite solar cells. *Nature* **628**, 93-98 (2024).

[S22] J. Li *et al.* Enhancing the efficiency and longevity of inverted perovskite solar cells with antimony-doped tin oxides. *Nat. Energy* **9**, 308-315 (2024).